RESEARCH ARTICLE

Case Study on Impact of Geometric Fill Factor on the Effectiveness of Organic Solar Cells

Ye Chan Kim ⓘ | Sung Jae Jeon | Nam Gyu Yang | Doo Kyung Moon ⓘ

Nano and Information Materials (NIMs) Laboratory, Department of Chemical Engineering, Konkuk University, Seoul, Republic of Korea

Correspondence: Doo Kyung Moon (dkmoon@konkuk.ac.kr)

ABSTRACT

This study investigates the impact of the geometric fill factor (GFF) on the practical performance of organic solar cell (OSC) modules fabricated by two distinct approaches: a conventional hand-made method and UV nanosecond laser patterning technique. Using the optimized PM6:L8-BO photoactive system, two OSC modules—each comprising three sub-cells—were fabricated under the same device dimensions (35×35 mm). Laser-patterned module exhibited a substantial enhancement in GFF from 62.73% to 98.41%, resulting in an increase in the maximum output power (P_{max}) from 69.67 mW to 124.25 mW. To evaluate the practical energy harvesting capability, capacitor-charging experiments were performed under identical illumination conditions. The laser-patterned module reached the target voltage of 2.5 V in 380 seconds, whereas the hand-made module required 610 s to reach the same voltage. These results demonstrate that a cost-effective UV nanosecond laser system can effectively optimize the GFF and nearly double the output power of OSC modules. Furthermore, comprehensive stability evaluations emphasize the importance of ensuring process reliability, highlighting the key technological challenges that must be addressed for future industrial implementation.

1 | Introduction

Organic solar cells (OSCs) have attracted considerable attention as one of the most promising emerging photovoltaic (PV) technologies, alongside dye-sensitized solar cells and perovskite solar cells (PSCs). Low-temperature solution-processable OSCs can be fabricated as lightweight, flexible devices, making them particularly well-suited for large-area modules produced through roll-to-roll printing. This approach offers distinct advantages for industrial-scale manufacturing [1, 2]. Furthermore, the tunable bandgap of organic semiconductors enables for high optical transparency and diverse color tunability, rendering OSCs suitable for applications such as building-integrated photovoltaics (BIPVs), vehicle-integrated photovoltaics (VIPVs), and smart window technologies [3, 4]. In addition, their high absorption coefficients enable excellent photovoltaic performance under indoor conditions, making them as promising candidates for autonomous indoor power sources in Internet of Things (IoT) devices and sensor systems [5]. Recent advancements in materials development and device engineering have enabled lab-scale OSCs to achieve power conversion efficiency (PCE) exceeding 20% at the unit cell level [6–9] and 16–17% at the mini-module level [10, 11].

Notably, Zhu et al. reported PCE of 20.8% in small-area devices (5.2 mm^2) and 17.0% in mini-modules (17.6 cm^2) by employing an additive-assisted layer-by-layer technique. This method promotes the formation of a bulk p-i-n structure and facilitates vertical phase segregation within the active layer, resulting in significant enhancements in light harvesting due to the wrinkle-patterned morphology. These findings highlight the potential of this innovative approach in improving the performance of OSCs for practical applications [12].

These advancements have broadened the applicability of OSCs beyond traditional outdoor solar energy harvesting, facilitating their use as independent power sources across a wide range of indoor and outdoor lighting conditions [13]. In addition, stable power generation under low illumination conditions (200–1000 lux) has been demonstrated in multiple studies, including the successful operation of self-powered IoT applications [14–16].

Recently, Wang et al. demonstrated a dicarbolong-phenanthroline-based OSC module that achieved a remarkable PCE of 30.6% under 1000 Lx LED illumination, thereby effectively utilizing indoor light for wireless power transfer. Notably, this module was successfully integrated with a commercial electronic shelf label (ESL) system, serving as a replacement for conventional batteries. The OSC modules were capable of charging a lithium battery (LIR2032) and refreshing the ESL display up to 13 times per day under continuous 500 Lx LED illumination. This suggests the practical application of OSCs in powering self-sustained IoT electronics under indoor conditions [17]. These findings underscore the practical viability of OSCs as reliable energy sources for next-generation self-powered electronic applications.

Building on these developments, the advancement of OSCs highlights that, beyond improving the efficiency of individual cells, research has increasingly focused on module-level optimization to facilitate industrial implementation. This transition from high-efficiency device development to application-driven research underscores the importance of a holistic approach to enhance the overall effectiveness and practicality of OSC technology. In particular, it is critical to design modules that maximize the active area, which refers to the effective area contributing to practical power generation, while simultaneously minimizing the electrically inactive region (dead zone) between sub-cells. The geometric fill factor (GFF) quantifies the proportion of the module area that effectively contributes to light harvesting. It is defined as follows:

$$GFF = \frac{\text{Active area}}{\text{Aperture area}} = \frac{W_a}{W_a + W_d} \qquad (1)$$

where W_a is the active area and W_d is the width of the dead zone. A higher GFF corresponds to a smaller proportion inactive area, thereby making it a critical parameter for evaluating the effective power output of PV modules [18–21]. Therefore, achieving a high GFF provides a practical strategy for enhancing output, even in cases where the intrinsic efficiency of individual unit cells is relatively low.

Design strategies aimed at improving the GFF are not limited to OSCs but are also widely applicable to other emerging PV technologies, including PSCs. For instance, Nikbakht et al. reported a fabrication process for perovskite modules using a 355 nm picosecond laser. During the P1 process, an ablation width of 10 μm was precisely defined on the transparent fluorine-doped tin oxide (FTO) electrode. The P2 step, which is responsible for establishing electrical connections between adjacent sub-cells, required the selective removal of all functional layers above the bottom FTO electrode. Given that any damage to the FTO could lead to the formation of Schottky junctions and an increase in series resistance, meticulous control over the patterning process was essential. To ensure complete removal of the functional layers without damaging the bottom electrode, six parallel laser patterning lines were employed, resulting in a clean ablation width of 120 μm. In the P3 step, the top metal electrode was selectively ablated to achieve electrical isolation between neighboring cells. The resulting large area, measuring 15.6 × 15.6 cm (total area: 243.4 cm^2), exhibited an aperture area of 156 cm^2 and an active area of 150.4 cm^2. This configuration resulted in a minimized dead zone of 180 μm, GFF of 96.4%, and PCE of 17.68% [21]. This study underscores that laser patterning not only enhances the GFF but also serves as a fundamental strategy for improving the practicality and scalability of emerging PV technologies.

In addition, Basu et al. conducted a finite element method simulation to optimize the module layout of a 143× 143 mm OSC module. Their analysis focused on the impact of cell number and cell width on both electrical and geometrical losses. According to their results, an increase in the number of cells leads to narrower cell widths, which effectively shortens the current path and reduces series resistance. However, this approach necessitates more frequent P1–P3 laser patterning, which increases the cumulative dead zone and decreases the GFF, ultimately reducing the effective area available for photovoltaic conversion. Conversely, reducing the number of cells decreases the number of patterning steps, thereby improving the GFF. However, this approach results in wider cell widths and increased series resistance, ultimately leading to degraded performance. Through simulations with varying cell counts ranging from 20 to 60, it was determined that a configuration comprising 38 cells, with a cell width of approximately 3.63 mm, provides the optimal trade-off between resistance and GFF losses. This configuration effectively maximizes the module's PCE based on the active layer of PM6:Y6-C12:PC$_{61}$BM. This study underscores that realizing high-efficiency large-area OSC modules requires meticulous optimization of cell width and patterning design, rather than merely scaling up module size [18].

In this study, we fabricated OSC modules using two distinct approaches: a conventional hand-made method and a UV nanosecond laser patterning technique. Notably, the PM6 (PCE > 15% batch with Y6) and the affordable laser-patterning machine were employed to improve the commercial viability of OSCs. In summary, the photovoltaic performance of OSC unit cells (active area: 0.04 cm^2) was optimized, achieving PCE of 16.09%. By comparing the photovoltaic performance of the resulting modules under identical material compositions and fabrication conditions, we evaluated the feasibility and process advantages of laser-based patterning techniques for scalable large-area manufacturing. In our modules, laser patterning increased the GFF from 62.73% to 98.41% and improved the P_{max} from 69.67 to 124.25 mW at identical dimensions. This improvement arises from minimizing the inter-cell dead zone, as discussed in detail in the following paragraphs.

To experimentally investigate the impact of the GFF on actual energy generation performance, we conducted a capacitor charging test using a 2.7 V, 3 F capacitor, which is commonly employed in low-power electronic devices. The capacitor was initially discharged a voltage below 0.2 V. Subsequently, the time required to charge it to 2.5 V was measured using both the hand-made and laser-processed modules. Both modules exhibited characteristic saturation-type charging behavior, characterized by a rapid initial increase in voltage, followed by a gradual reduction in the charging rate. However, the hand-made module required approximately 610 s to reach 2.5 V, while the laser module, which exhibited nearly double the P_{max}, reached the same voltage in only 380 s. Importantly, this work demonstrates that a cost-effective UV nanosecond laser, when combined with the high-performance PM6:L8-BO system, enables the reduction of the dead zone from 4.8 mm to 136 μm and the quantitative improvement of GFF from 62.7% to 98.4%, providing an industrially scalable route for high-performance OSC modules.

2 | Results and Discussion

Figure 1 presents the overall structure of OSC modules fabricated in this study, including the chemical structures of the constituent materials. Additionally, it provides a comparative analysis of the geometry and performance of two distinct modules fabricated using hand-made and laser-patterned methods. As illustrated in Figure 1a,b, the OSCs employed a conventional device architecture with the configuration of indium tin oxide (ITO)/poly(3,4-(hylenedioxythiophene):polystyrene sulfonate (PEDOT:PSS)/PM6:L8-BO/N, N′-Bis{3-[3-(dimethylamino)propylamino]propyl}perylene-3,4,9,10-tetracarboxylic diimide (PDINN)/Ag. This structure is generally well-suited for high-efficiency OSC devices fabricated using solution-processing techniques. In this configuration, PEDOT:PSS functions as the hole transport layer (HTL), PM6:L8-BO serves as the photoactive layer, and PDINN acts as the electron transport layer (ETL).

The fundamental optoelectronic characteristics of the active materials, such as PM6 and L8-BO, including cyclic voltammetry (CV) curves, UV–Vis normalized absorption spectra, and the corresponding energy level diagram, are provided in Figure S1. Based on the CV and UV–Vis absorption analyses of PM6 and L8-BO, the highest occupied molecular orbital (HOMO) and lowest unoccupied molecular orbital (LUMO) energy levels were determined to be −5.54 and −3.73 eV for PM6, and −5.68 and −3.90 eV for L8-BO, respectively. This well-aligned energy level configuration is expected to facilitate efficient charge transfer between the donor and acceptor. Furthermore, the optical bandgaps of PM6 and L8-BO were calculated to be 1.82 and 1.43 eV, respectively, corresponding to a complementary photon-harvesting range of 400–900 nm. These characteristics are anticipated to contribute to the achievement of high-performance OSCs by providing high open-circuit voltage (V_{OC}) and short-circuit current density (J_{SC}). The correlation between such favorable energy level alignment and the simultaneous enhancement of V_{OC} and J_{SC} has been documented in multiple studies [22–24]. For example, Shen et al. reported that the well-matched HOMO/LUMO alignment in PM6:L8-BO devices improved charge transport and suppressed recombination, thereby enhancing both V_{OC} and J_{SC} [22].

To establish the optimal processing conditions prior to module-scale fabrication, 0.04 cm^2 unit-cell was fabricated based on the conventional configuration illustrated in Figure 1a, incorporating a PM6:L8-BO blend as the photoactive layer. With the exception of the Ag top electrode, all layers were deposited using spin-coating to ensure uniformity and reproducibility through solution processing. As summarized in supporting information Table S1, the optimized unit-cell device exhibited PCE of 16.09%, with V_{OC} of 0.845 V, J_{SC} of 24.90 mA cm^{-2}, and fill factor (FF) of 76.44%.

Based on this optimized unit-cell protocol, series-connected OSC modules were fabricated on 35 × 35 mm ITO glass substrates under identical processing conditions while differing only in the P1–P3 patterning steps. One module was produced using a conventional wet-etching, hand-made process [25], and the other was prepared using a precision UV nanosecond laser patterning method; the two modules were subsequently compared in terms of their photovoltaic performance and geometric characteristics. This laser patterning-based approach enables complete P1–P3 patterning without additional masking or mechanical processing, thereby simplifying the fabrication process and significantly minimizing the dead zone between adjacent cells. The resulting geometric differences of two modules are clearly illustrated in Figure 1c and S2a. By minimizing the inactive spacing, the laser-patterned modules allow more efficient utilization of the aperture area, which directly leads to a higher GFF. To achieve this, the P1–P3 patterning parameters were systematically optimized, and the optimization procedures along with their characterization results are described in detail in the following section.

Figure 2 illustrates the overall fabrication process of OSC modules based on UV nanosecond laser patterning, together with the corresponding scribed patterns and optical analyses of the laser-patterned regions. Figure 2a shows the overall process flow for fabricating series-connected OSC modules, demonstrating that all P1–P3 patterning steps can be performed using only UV nanosecond laser system, as discussed in the following section.

Figure 2b presents a cross-sectional schematic of the completed laser-patterned module, which consists of three series-connected sub-cells. Each sub-cell has an active area of approximately
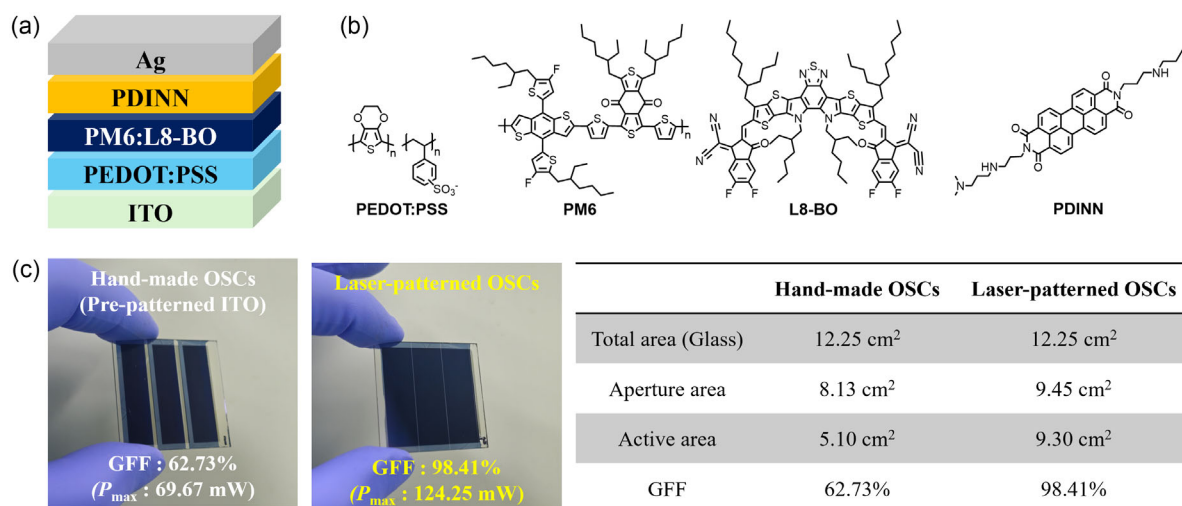

	Hand-made OSCs	Laser-patterned OSCs
Total area (Glass)	12.25 cm^2	12.25 cm^2
Aperture area	8.13 cm^2	9.45 cm^2
Active area	5.10 cm^2	9.30 cm^2
GFF	62.73%	98.41%

FIGURE 1 | (a) Schematic diagram of the conventional device structure of OSCs. (b) Chemical structures of the materials used in each layer. (c) Photographs of OSC modules fabricated using the hand-made method and the laser-patterning technique.
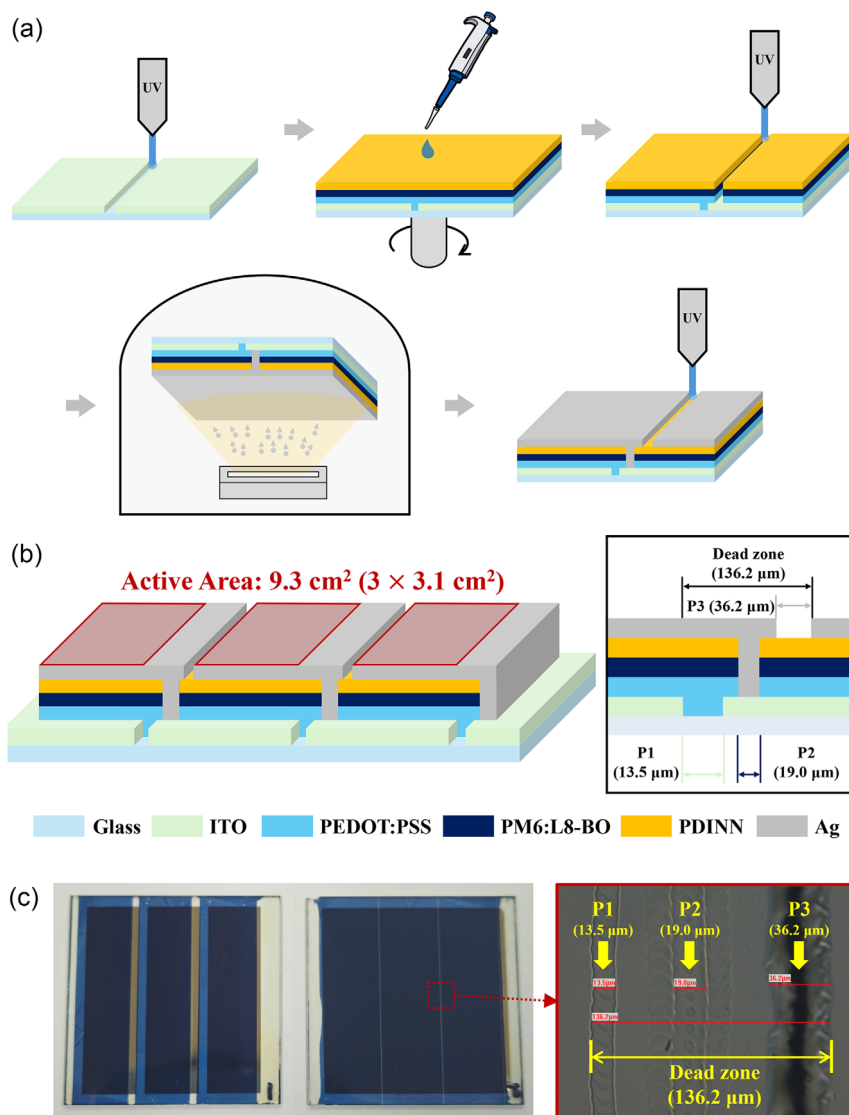
FIGURE 2 | (a) Process flow for the fabrication of OSC modules using UV nanosecond laser patterning, which includes three stages: P1 (ITO patterning), P2 (removal of the active and buffer layers), and P3 (Ag electrode patterning). (b) Cross-sectional schematic of the completed laser-patterned module produced using a laser patterning machine. (c) Optical image of the fabricated hand-made and laser-patterned OSC modules, accompanied by microscopic analysis results detailing the widths of the laser patterning.

3.1 cm^2, resulting in a total active area of 9.3 cm^2. As highlighted in the enlarged schematic, the laser patterning widths were precisely controlled as P1 $\approx$ 13.5 μm, P2 $\approx$ 19.0 μm, and P3 $\approx$ 36.2 μm, leading to a minimized overall dead zone width of about 136.2 μm. This represents more than a 35-fold reduction compared to the 4.8 mm dead zone observed in the hand-made method (Figure S2), quantitatively demonstrating the superior capability of laser patterning in minimizing inactive regions. Finally, Figure 2c provides optical images of both hand-made and laser-patterned OSC modules, along with microscopic images of the laser-scribed regions.

To further clarify and optimize the fabrication process described in Figure 2, the detailed laser patterning condition optimization results summarized in the Supporting Information (Figure S3–S6, Table S2–S3) are discussed. The laser patterning procedure consists of three sequential steps: P1, isolation of the bottom ITO electrode; P2, selective removal of the photoactive and buffer layers; and P3, isolation of the top Ag electrode. All three steps

can be performed using UV nanosecond laser system without the need for masking or wet-etching processes. This enables a simplified, noncontact, and highly precise fabrication process with excellent reproducibility.

To define the process window, the fundamental effects of Q-pulse width and scan speed on energy distribution and overlap behavior are conceptually illustrated in Figure S3. A shorter pulse (e.g., 5 μs) delivers higher peak energy density, resulting in aggressive ablation, whereas a longer pulse (e.g., 10 μs) spreads the energy over time, leading to insufficient material removal. Likewise, a lower scan speed increases the degree of pulse overlap, while a higher speed decreases it, directly influencing line uniformity and edge continuity. Building on this concept, the experimental influence of pulse width on the ablation characteristics was examined for the P1 isolation process, as shown in Figure S4. The ablation morphology systematically changed with pulse width (8–16 μs): shorter pulses produced excessive ablation and damage, whereas longer pulses resulted in incomplete

isolation. Similarly, the effect of scan speed on the continuity and precision of the scribed lines was investigated and is presented in Figure S5. At low speeds (200–300 mm s^{-1}), sufficient overlap between adjacent laser spots generated uniform and well-connected isolation lines, while higher speeds (≥700 mm s^{-1}) produced discontinuous or irregular patterns. An optimized scan speed of 300 mm s^{-1} achieved the best balance between throughput and pattern quality. Furthermore, the optimization results for the P2 and P3 steps are presented in Figure S6 and Tables S2–S3, respectively. These results experimentally demonstrate that the conventional wet-etching-based P1, hand-made P2, and shadow-mask-patterned P3 processes can all be fully replaced by UV nanosecond laser-based approach. The laser-integrated P1–P3 process exhibits sufficient reliability and reproducibility, confirming its feasibility as a practical and credible alternative to conventional manual and mask-based fabrication methods.

To evaluate the effect of laser patterning precision on the photovoltaic performance, the current–voltage (J–V) characteristics of the two OSC modules were analyzed, as summarized in Figure 3a,b and Table 1. A detailed summary of geometry-dependent parameters, including the dead-zone width, GFF, and P_{max}, is additionally provided in Table S4 to complement these electrical comparisons. The measurements were performed both with and without a shadow mask to quantitatively assess the influence of the interconnection patterning method on the electrical behavior and output characteristics of the modules. This methodology accounts for the geometric losses inherent to the module layout and thus provides a more realistic evaluation of device performance under actual operating conditions [26].

Under a shadow mask area of 4.725 cm^2, the hand-made module exhibited V_{OC} of 2.67 V, J_{SC} of 7.41 mA cm^{-2}, FF of 71.65%, P_{max} of 66.89 mW, and PCE of 14.16%. In contrast, the laser-patterned module demonstrated V_{OC} of 2.640 V, J_{SC} of 7.53 mA cm^{-2}, FF of 73.13%, P_{max} of 68.66 mW, and PCE of 14.53%. The notable improvement in FF can be attributed to enhanced interconnection uniformity and effective suppression of shunt-related losses through precise laser patterning [27]. When measured without a shadow mask, the hand-made module showed an active area of 5.1 cm^2 with PCE of 13.66%, V_{OC} of 2.64 V, J_{SC} of 7.40 mA cm^{-2}, FF of 69.94%, P_{max} of 69.67 mW, and GFF of 62.73%. Meanwhile, the laser-patterned module exhibited an active area of 9.3 cm^2, PCE of 13.36%, despite having a larger active area of 9.3 cm^2, with V_{OC} of 2.68 V, J_{SC} of 7.45 mA cm^{-2}, FF of 66.99%, P_{max} of 124.25 mW, and GFF of 98.41%.

A slight reduction in efficiency was observed for the laser-patterned module, likely due to the thickness gradient of the active layer induced by the coffee-ring effect during the spin-coating process. This thickness nonuniformity is expected to have a more pronounced impact on modules with larger GFF values. Employing alternative coating techniques such as blade coating or slot-die coating could mitigate these issues by improving film uniformity, potentially enabling further enhancements in module efficiency. Additionally, the increased sheet resistance of the ITO electrode associated with the enlarged active area could also contribute to the reduced PCE [28]. Nevertheless, the laser-patterned module demonstrated a remarkably enhanced P_{max}, driven n by its high GFF, which is particularly beneficial from an industrial perspective where absolute output power of the hand-made module.

In addition, Figure 3c–f further elucidates the electrical behavior of the two modules. As shown in Figure 3c, the laser-patterned module exhibits a lower leakage current in the dark current curve compared to the hand-made module, indicating an enhanced diode quality attributed to the more precise patterning [29]. Figure 3d illustrates the photocurrent density (J_{ph}) as a
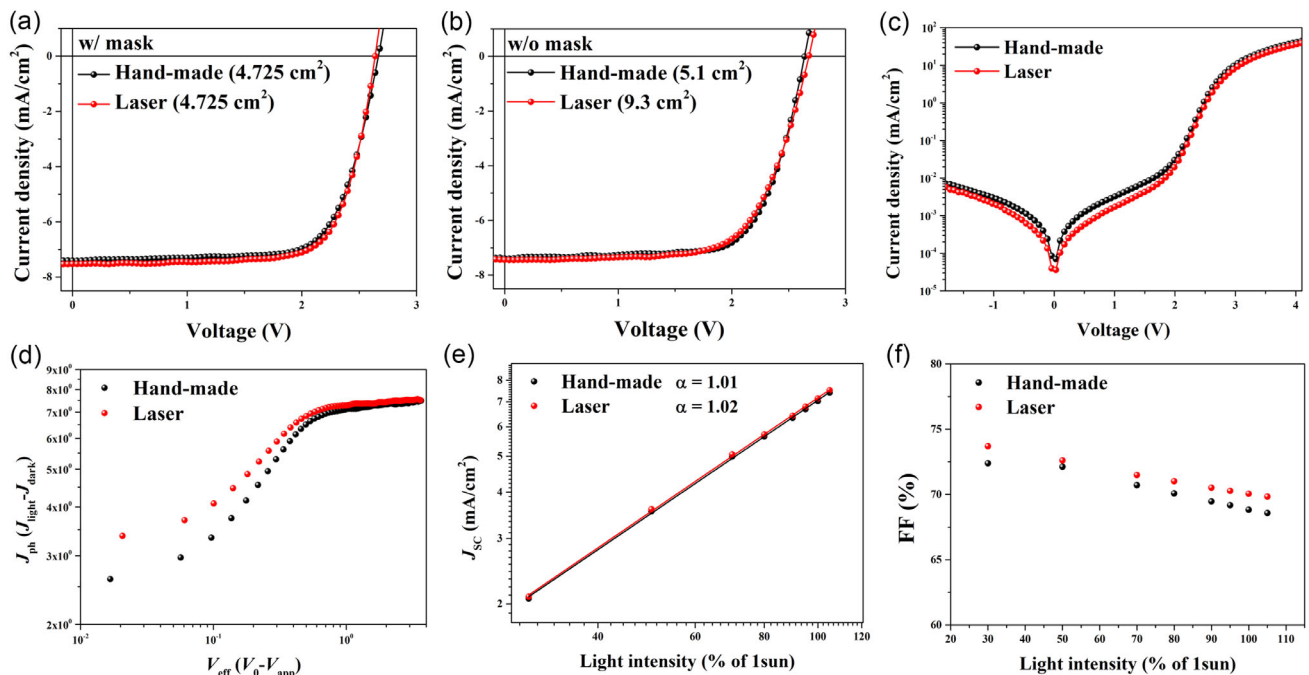

FIGURE 3 | J–V characteristic curves of hand-made and laser-scribed OSC modules measured (a) with and (b) without a shadow mask: each inset provides details on the processing method and effective active area for both modules. (c) Dark current, (d) J_{ph}–V_{eff} plots, and light intensity versus (e) J_{SC} and (f) FF characteristics.

TABLE 1 | Photovoltaic performance parameters of hand-made and laser-scribed OSC modules under AM 1.5G illumination (100 mW cm^{-2}), measured with and without a shadow mask.

Materials[a]	Shadow mask	Active area (cm²)	Patterning method	V_{OC} (V)	J_{SC} (mA cm^{-2})	FF (%)	P_{max} (mW)	R_s (Ω)	R_{sh} (Ω)	PCE (%)	GFF (%)
PM6:L8-BO	O	4.725 [3 cells]	Hand-made	2.67 (2.67 ± 0.01)	7.41 (7.27 ± 0.14)	71.65 (71.38 ± 0.90)	66.89 (65.49 ± 1.11)	11.39 (11.76 ± 0.38)	2128.78 (2715.41 ± 1270.76)	14.16 (13.86 ± 0.24)	
		4.725 [3 cells]	Laser	2.640 (2.621 ± 0.01)	7.53 (7.396 ± 0.139)	73.13 (73.12 ± 0.85)	68.66 (66.97 ± 1.21)	9.89 (10.00 ± 0.42)	3251.14 (3232.97 ± 2440.76)	14.53 (14.172 ± 0.25)	
	X	5.1 [3 cells]	Hand-made	2.64 (2.64 ± 0.02)	7.40 (7.29 ± 0.06)	69.94 (68.57 ± 0.92)	69.67 (67.16 ± 1.33)	11.44 (11.46 ± 0.55)	1904.23 (1194.97 ± 504.92)	13.66 (13.17 ± 0.26)	62.73
		9.3 [3 cells]	Laser	2.68 (2.66 ± 0.01)	7.45 (7.30 ± 0.07)	66.99 (67.35 ± 0.44)	124.25 (121.34 ± 1.67)	7.25 (7.35 ± 0.14)	1157.25 (1928.02 ± 1582.41)	13.36 (13.05 ± 0.18)	98.41

aAverage values and standard deviations calculated from 9 individual devices.

function of the effective voltage (V_{eff}). The laser-patterned module reaches saturation current more rapidly than the hand-made module, indicating enhanced charge extraction efficiency and reduced recombination losses [30]. Figure 3e presents the J_{SC} as a function of light intensity on a log–log scale. Both modules exhibit power-law exponents (α) of 1.01 and 1.02, respectively, suggesting near-ideal photovoltaic behavior with minimal bimolecular recombination under varying illumination conditions [31]. Lastly, Figure 3f shows the FF as a function of light intensity, demonstrating that the laser-patterned module consistently exhibits a higher and more stable FF throughout the entire illumination range compared to the hand-made module. According to previously reported studies, this trend suggests that the laser-patterning process can reduce series resistance and improve interfacial contact properties [32].

Importantly, since the two modules share identical device structures and processing conditions, they differ only in the series-connection patterning method. Therefore, the observed performance improvements can primarily be attributed to enhanced inter-electrode contact and minimization of the dead zone. Supporting this conclusion, the series resistance (R_s) decreased from 11.39 Ω in the hand-made module to 9.89 Ω in the laser-patterned one, while the shunt resistance (R_{sh}) increased significantly from 2128.78 to 3251.14 Ω. These changes confirm that the laser-patterned process effectively reduces contact resistance and consequently recombination losses [33].

To further demonstrate the practical applicability of the low-cost OSC modules fabricated using an inexpensive active-layer polymer and a cost-effective laser process, we evaluated their photovoltaic performance under indoor light conditions ranging from 10,000 to 200 Lx. As summarized in Table S5, the laser-patterned module exhibited consistently higher efficiency than the hand-made module in the medium-to-high illumination range ($\geq$250 Lx), consistent with the trend observed under AM 1.5G illumination. However, as the illumination intensity decreased, the performance gap between the two modules gradually narrowed, and although the laser-patterned module maintained a slightly higher PCE (13.95%) than the hand-made module (13.45%) under 1 sun, the efficiency was eventually reversed at 200 Lx. This trend closely correlates with the resistance behavior summarized in Table S6. The R_s of the laser-patterned module, which was lower than that of the hand-made module under high illumination, progressively increased with decreasing light intensity and became more than twice as large at 200 Lx. This behavior is consistent with the efficiency crossover observed under indoor lighting. In addition, the laser-patterned module exhibited consistently lower R_{sh} than the hand-made module across the entire illumination range (10,000–200 Lx), indicating that leakage losses through defect-mediated regions were more significant. Such leakage can be attributed to line-edge corrosion and localized thermal and chemical damage induced by the laser scribing process, which likely introduces recombination sites not only in the photoactive layer but also in the HTL and ETL organic semiconductor structures. Nevertheless, under relatively high illumination levels ($\geq$10,000 Lx), the laser-patterned module maintained a higher shunt resistance than the hand-made counterpart, suggesting that recombination losses associated with the laser process do not dominate device performance when carrier generation is sufficiently strong.

In response to the growing industrial demand for eco-friendly processing, OSC modules were fabricated using the nonhalogenated solvent o-xylene [34]. To further demonstrate the universality of the laser patterning process capable of achieving a GFF above 98%, we evaluated the photovoltaic performance and light stability of o-xylene-processed OSC modules. The results revealed that the o-xylene-based devices exhibited photovoltaic characteristics comparable to those of conventional CF-based OSC modules fabricated using halogenated solvents. Notably, the o-xylene-processed modules showed superior photostability compared with their CF-based counterparts. The detailed data are provided in Table S7 and Figure S7 of the Supporting Information.

Figure 4 presents the stability test results of the two modules evaluated under the three standard ISOS protocols: ISOS-D-1, ISOS-D-2, and ISOS-L-1. Under ISOS-D-1 (dark, N_2, 25°C), both modules retained more than 95% of their initial efficiency over 140 h, confirming that the laser-patterning process did not introduce additional defects or instability within the devices. Under ISOS-D-2 (dark, 85°C), a slight burn-in behavior was observed during the first 10 h, followed by a gradual decay, with both modules exhibiting a similar T_{80} lifetime of approximately 70 h. This result indicates that the electrode–interface contacts in the laser-patterned module remained thermally stable under high-temperature stress without any notable charge recombination or metal diffusion. In contrast, ISOS-L-1 (ambient, LED illumination) revealed a relatively faster light-induced degradation. Both modules reached the T_{80} point within 8 h, with the laser-patterned module exhibiting a slightly faster decline. This behavior is more likely related to pulse-induced surface damage generated during the laser-patterning process rather than to thermal effects. Pou-Álvarez et al. systematically compared nanosecond, picosecond, and femtosecond laser treatments on metallic surfaces. They reported that nanosecond laser, owing to their relatively long pulse duration and strong thermal diffusion, produced thicker recast layers, melt ejection features, and rougher grooves, which increased the surface oxidation and corrosion susceptibility under ambient conditions. In contrast, picosecond laser generated more uniform ablation profiles with limited thermal effects, while femtosecond laser enabled almost nonthermal material removal, resulting in smoother and cleaner surfaces with superior corrosion resistance [35]. In the present study, the UV-nanosecond laser used for module fabrication may have induced a similar morphology modification—particularly increased edge roughness and reactive sites—leading

to a slightly faster degradation under light exposure, as observed in the ISOS-L-1 stability test. In contrast, the hand-made module fabricated via shadow-mask deposition retained a smoother electrode interface and consequently exhibited higher stability against oxygen- and moisture-induced degradation. Overall, the laser-patterned modules exhibited comparable stability to the hand-made counterparts under storage (D-1) and thermal (D-2) conditions, whereas the faster degradation observed under light (L-1) conditions may be partially attributed to localized surface damage from high-energy laser pulses. These findings suggest that pulse-energy optimization and surface post-treatment or passivation could mitigate such effects and further enhance the long-term photostability of laser-processed OSC modules.

To mitigate the degradation of laser-patterned modules and improve process reliability, refinement of the beam profile should be considered. According to the report by Rung et al., a Gaussian beam, which is typically employed in most nanosecond laser systems, exhibits a pronounced central intensity peak that often leads to local overheating, recast layer formation, and edge roughening. In contrast, a top-hat (flat-top) beam provides a more uniform energy distribution across the irradiation area, thereby resulting in smoother ablation, reduced tapering, and a smaller heat-affected zone (HAZ), as widely reported in laser micromachining studies [36].

Therefore, implementing a beam homogenizer or diffractive optical element to achieve such a top-hat beam profile could minimize ablation nonuniformity and suppress the formation of corrosion-prone sites on the electrode surface, even under high-energy UV nanosecond operation.

Figure 5 presents a comparative evaluation of the practical output power and energy storage efficiency of hand-made and laser-patterned OSC modules, as assessed through a capacitor charging experiment. This test was designed to quantitatively evaluate the power delivery capabilities of each module by monitoring the charging behavior of an external capacitor, which is driven by the photocurrent generated from the OSC. Specifically, Figure 5a illustrates the schematic diagram of the charging circuit, in which a 2.7 V, 3 F capacitor is directly charged by the OSC module. The voltage variation is recorded in real-time using a digital multimeter, which is connected to a PC via USB for automated data logging through dedicated software. This measurement setup closely resembles the solar-charging power unit configuration proposed by Jin et al., which integrates power generation and storage in real-time [37].
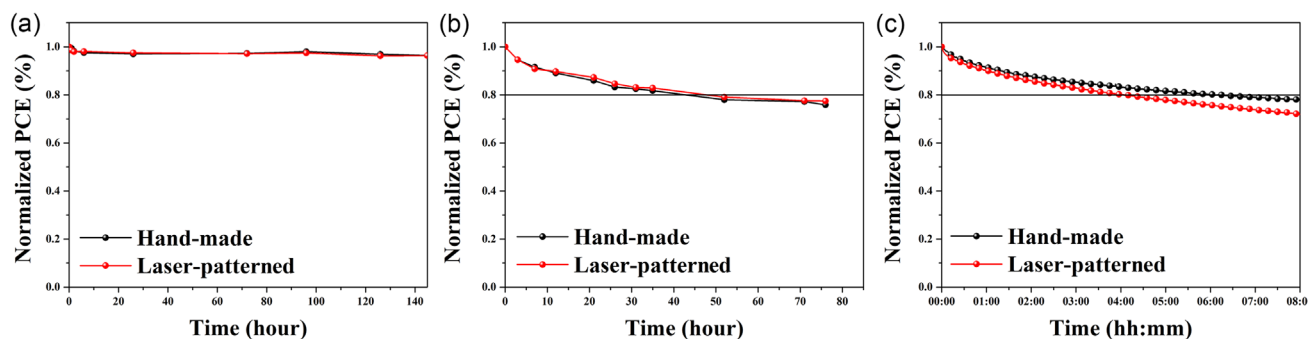
FIGURE 4 | Stability test results of hand-made (black) and laser-patterned (red) OSC modules under different ISOS protocols. (a) ISOS-D-1: N_2 atmosphere, dark, 25°C, (b) ISOS-D-2: N_2 atmosphere, dark, 85°C, (c) ISOS-L-1: ambient air, LED illumination (1 sun), 25°C. All devices were tested without encapsulation; for D-2 and L-1, the performance was monitored until it decreased to 80% of the initial value (T_{80}).
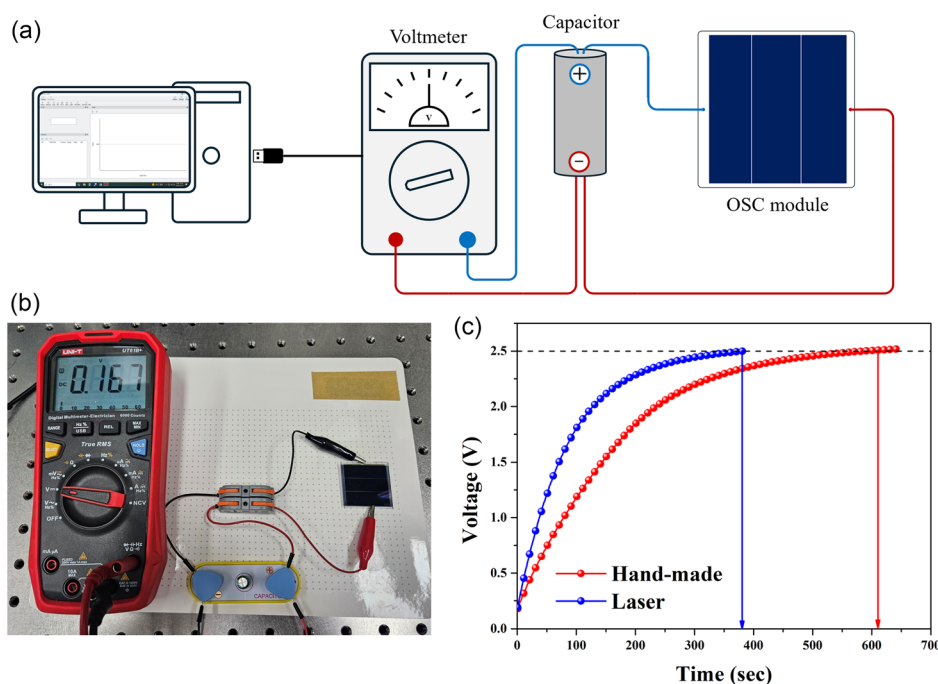
FIGURE 5 | (a) Schematic diagram of the capacitor charging setup using an OSC module. (b) Photograph of the capacitor charging system incorporating the laser-patterned module. (c) Charging curves of capacitors powered by two distinct OSC modules.

Subsequently, Figure 5b displays a photograph of the actual experimental setup, illustrating the series connection of the laser-patterned OSC module, capacitor, and measurement devices. Regarding charging performance, the results in Figure 5c clearly indicate that the laser-patterned module exhibits a faster initial charging rate and superior power delivery efficiency compared to its hand-made counterpart. As the voltage across the capacitor approaches the V_{OC} of the module, the voltage difference that drives current through the circuit diminishes. This results in a gradual reduction in the charging current, which is a typical behavior of capacitor-based charging systems. This characteristic supports the conclusion that laser-based precision patterning not only enhances cell-level efficiency but also facilitates faster and more stable energy transfer when integrated with storage components. Therefore, this experiment quantitatively demonstrates that the laser-patterned OSC module outperforms the hand-made module in terms of both output power and dynamic charging response. This finding underscores the effectiveness of precision laser patterning in improving not only intrinsic photovoltaic performance but also the system-level compatibility. Furthermore, this approach provides a practical and reliable experimental framework for evaluating power delivery dynamics in the design of module-based energy harvesting and storage systems.

As summarized in Table S8, the UV nanosecond laser-patterned module developed in this study achieved a high GFF of 98.4% and a comparable efficiency of ∼13%, despite utilizing a low-cost laser system. Although femtosecond laser processing enables highly precise patterning and excellent device performance, its prohibitively high equipment cost remains a major obstacle for industrial adoption.

In contrast, the nanosecond laser system provides a much simpler configuration and lower operational cost while maintaining sufficient fabrication precision, rendering it more suitable for large-area module manufacturing and scalable industrial implementation. Therefore, the proposed strategy offers a well-balanced compromise between performance and process scalability, establishing a practical and economically viable alternative that bridges the gap between high-cost femtosecond processing and cost-effective industrial production.

3 | Conclusion

In this study, the UV nanosecond laser patterning process was optimized to achieve GFF of 98.41%, resulting in reduced electrical losses and nearly doubled output power compared with the hand-made module. Stability assessments under the ISOS-D-1, D-2, and L-1 protocols indicated that both modules exhibited comparable thermal and storage stability, while the laser-patterned module showed slightly faster degradation under illumination. This behavior is presumed to result from localized thermal effects that may induce surface roughening and interfacial deterioration, suggesting that laser parameter optimization, beam homogenization, and interfacial passivation could further improve durability. Under indoor illumination, the laser-patterned module exhibited higher performance in the range of 10,000 to 250 Lx compared with the hand-made module; however, at 200 Lx, an increase in the series resistance of the laser-patterned module led to a performance reversal, with the hand-made module exhibiting slightly higher efficiency. This result may be attributed to line-edge degradation induced by the laser patterning process. Additionally, OSC modules fabricated using the eco-friendly, nonhalogenated solvent o-xylene confirmed that the proposed laser patterning process is stably applicable to green-solvent-based systems. Overall, this work demonstrates that a cost-effective and industrially scalable UV nanosecond laser patterning process can simultaneously achieve

high geometric precision, excellent photovoltaic performance, long-term operational stability, and environmental compatibility.

4 | Experimental Section

4.1 | Hand-Made Method (see Figure S2a)

The devices had a conventional ITO/PEDOT:PSS/PM6:L8-BO/PDINN/Ag structure. The P1 pattern was designed to fit within 35×35 mm ITO glass substrate, following a specified layout. The P1 pattern was prefabricated using a wet etching process (AMG), which established the fundamental structure for the sub-cells of the module. The line spacing is 2.2 mm. The ITO glass substrates were cleaned by ultrasonication in a sequence of Alconox, acetone (Ace), and isopropyl alcohol (IPA), with each step lasting 10 min each. The substrates were heat-treated on a hot plate at 100°C to remove residual moisture, followed by UV-ozone treatment (Ahtech LTS AH 1700) for 15 min. As a HTL, PEDOT:PSS (Heraeus, AI4083) solution was diluted with deionized (DI) water at a 5:1 volume ratio, filtered through a 0.45 μm PTFE filter, and then spin-coated onto ITO substrates at 4000 rpm for 30 s. The PEDOT:PSS-coated substrates were subsequently annealed at 110°C for 10 min. For the photoactive layer (AL) blend solution, the PM6 and L8-BO were dissolved in a solvent mixture of chloroform (CF):1,8-diiodooctane (DIO) (99.75:0.25, v/v), resulting in a total concentration of 15.4 mg/mL. For the eco-friendly condition, o-xylene (XY):diiodomethane (DIM) (99.75:0.25, v/v) was used as the solvent mixture with a total concentration of 24.2 mg mL^{-1}. In both cases, the donor-to-acceptor weight ratio was maintained at 1:1.2 (wt/wt). All prepared solutions were pre-heated to 80°C (CF-based) and 100°C (XY-based) and stirred for 3 h at 500 rpm using a magnetic stirrer. Prior to spin-coating, the active blend solution was gently cooled to 45°C for 10 min. The solution was then spin-coated onto the PEDOT:PSS surface at 3000 rpm for 30 s to form a 100 nm photoactive layer, which was subsequently thermally annealed at 80°C for 5 min. As an ETL, a 1 mg/mL solution of PDINN in methanol was subsequently spin-coated onto the photoactive layer at 2000 rpm for 30 s. No additional heat treatment was conducted. After then, P2 was manually patterned using a cotton swab to create a line approximately 1 mm wide, resulting in the exposure of the ITO electrode. Finally, Ag was thermally evaporated through a metal mask at a pressure of 10^{-7} torr with a thickness of 100 nm. This process resulted in the patterning of P3 with a line width of 1.5 mm, thereby completing the device fabrication.

4.2 | Laser Patterning Method (see Figure S2a)

For the laser-patterned modules, nonpatterned ITO glass substrates (35×35 mm) were processed using a UV nanosecond laser system controlled by EZCAD2 software. The operating parameters, including Q-pulse width and scan speed, were optimized for each patterning step (P1–P3) to ensure stable and precise patterning. P1 patterning was performed using a 355 nm UV nanosecond laser, with the following optimized parameters: a scan speed of 300 mm s^{-1}, a frequency of 48 kHz, and a Q-pulse width of 13 μs. The laser-scribed substrates were then cleaned following the same cleaning protocol as that used in the hand-made method. This process included sequential ultrasonication in Alconox, acetone, and IPA, followed by thermal and UV-ozone treatments.

Subsequently, the HTL (PEDOT:PSS), AL (PM6:L8-BO), and ETL (PDINN) were deposited using the same procedures used as those employed for the hand-made devices. After completing all coating steps, P2 patterning was conducted using a UV laser with a scan speed of 400 mm s^{-1} and a Q-pulse width of 16.5 μs to expose the ITO electrode. The Ag top electrode was then thermally evaporated without a shadow mask, following the same conditions as the hand-made method (100 nm thickness at a base pressure of 10^{-7} Torr). Finally, P3 laser patterning was performed at a scan speed of 300 mm s^{-1} and a Q-pulse width of 17.0 μs, thereby completing the fabrication of the serially connected OSC modules.

Conflicts of Interest

The authors declare no conflicts of interest.

Data Availability Statement

The data that support the findings of this study are available in the supplementary material of this article.

References

1. S. A. Hashemi, S. Ramakrishna, and A. G. Aberle, "Recent Progress in Flexible-Wearable Solar Cells for Self-Powered Electronic Devices," *Energy & Environmental Science* 13 (2020): 685.

2. J. Zhu, J. Xia, Y. Li, and Y. Li, "Perspective on Flexible Organic Solar Cells for Self-Powered Wearable Applications," *Acs Applied Materials & Interfaces* 17 (2025): 5595.

3. S. J. Jeon, Y. C. Kim, J. Y. Kim, et al., "Molecular Design of Cost-Effective Donor Polymers with High Visible Transmission for Eco-Friendly and Efficient Semitransparent Organic Solar Cells," *Chemical Engineering Journal* 472 (2023): 144850.

4. S. Feroze, A. Distler, L. Dong, et al., "Long Term Outdoor Performance Evaluation of Printed Semitransparent Organic Photovoltaic Modules for BIPV/BAPV Applications," *Energy & Environmental Science* 18 (2024): 674.

5. J. Liu, Y. Cui, Y. Zu, et al., "Organic Photovoltaic Cells for Low Light Applications Offering New Scope and Orientation," *Organic Electronics* 85 (2020): 105798.

6. T. Tosc, "Single-Junction Organic Solar Cells with a Power Conversion Efficiency of More than 20%," *Nature Energy* 9 (2024): 930.

7. H. Chen, Y. Huang, R. Zhang, et al., "Organic Solar Cells with 20.82% Efficiency and High Tolerance of Active Layer Thickness through Crystallization Sequence Manipulation," *Nature Materials* 24 (2025): 444.

8. R. Sun, X. Yuan, X. Yang, et al., "Cost-Efficient Recycling of Organic Photovoltaic Devices," *Joule* 8 (2024): 2523.

9. Y. Jiang, S. Sun, R. Xu, et al., "Non-Fullerene Acceptor with Asymmetric Structure and Phenyl-Substituted Alkyl Side Chain for 20.2% Efficiency Organic Solar Cells," *Nature Energy* 9 (2024): 975.

10. Z. Liu, Y. Fu, J. Wu, et al., "Removable Additive Assists Blade-Coated Large-Area Organic Solar Cell Modules Fabricated with Non-Halogenated Solvents Achieving Efficiency Over 16%," *Advanced Functional Materials* 35 (2025): 2401558.

11. H. Hu, Z. Jin, J. Ge, et al., "17.68% Efficiency Nonhalogenated Solvent-Processed Organic Solar Cell Modules Driven by Seed Crystal Strategy," *Advanced Materials* 37 (2025): 2420308.

12. L. Zhu, M. Zhang, G. Zhou, et al., "Achieving 20.8% Organic Solar Cells via Additive-Assisted Layer-by-Layer Fabrication with Bulk p-i-n Structure and Improved Optical Management," *Joule* 8 (2024): 3153.

13. M. Jahandar, S. Kim, and D. C. Lim, "Indoor Organic Photovoltaics for Self-Sustaining IoT Devices: Progress, Challenges and Practicalization," *ChemSusChem* 14 (2021): 3449.

14. D. Lübke, P. Hartnagel, J. Angona, and T. Kirchartz, "Comparing and Quantifying Indoor Performance of Organic Solar Cells," *Advanced Energy Materials* 11 (2021): 2101474.

15. E. Jiang, A. Jamali, M. List, et al., "Organic Photovoltaic Mini-Module Providing More than 5000 V for Energy Autonomy of Dielectric Elastomer Actuators," *Nature Communications* 16 (2025): 2048.

16. S. Mishra, S. Ghosh, B. Boro, et al., "Solution-Processed Next Generation Thin Film Solar Cells for Indoor Light Applications," *Energy Advances* 1 (2022): 761.

17. W. Wang, Y. Cui, Y. Yu, et al., "Indoor Organic Photovoltaic Module with 30.6% Efficiency for Efficient Wireless Power Transfer," *Nano Energy* 128 (2024): 109893.

18. R. Basu, F. Gumpert, J. Lohbreier, et al., "Large-Area Organic Photovoltaic Modules with 14.5% Certified World Record Efficiency," *Joule* 8 (2024): 970.

19. E. Feng, C. Zhang, J. Chang, et al., "A 16.10% Efficiency Organic Solar Module with Ultra-Narrow Interconnections Fabricated via Nanosecond Ultraviolet Laser Processing," *Cell Reports Physical Science* 5 (2024): 101883.

20. C. Han, Z. Jin, C. Shen, et al., "Green-Solvent-Processed Scalable Semi-Transparent Organic Solar Modules with 9.4% Efficiency and 42% Visible Transparency for Energy-Generating Windows," *Advanced Energy Materials* 15 (2025): 2501682.

21. H. Nikbakht, P. Mariani, L. Vesce, et al., "Upscaling Perovskite Photovoltaics: From 156 cm2 Modules to 0.73 M2 Panels," *Advancement of Science* 12 (2025): 2416316.

22. X. Shen, X. Wang, J. Wang, et al., "Efficient and Easily Repeatable Organic Solar Cells in a High Boiling Point Solvent by Introducing a Highly Mixed Tolerant Guest Acceptor," *Journal of Materials Chemistry C* 12 (2024): 17403.

23. C. Chen, L. Wang, W. Xia, et al., "Molecular Interaction Induced Dual Fibrils towards Organic Solar Cells with Certified Efficiency over 20%," *Nature Communications* 15 (2024): 6865.

24. Z. Wen, R. Zhou, Z. Zheng, and Y. Zhao, "PM6/L8-BO Thin Films through Layer-by-Layer Engineering: Formation Mechanism, Energetic Disorder, and Carrier Mobility," *Aggregate* 6 (2025): e729.

25. Y. C. Kim, S. J. Jeon, N. G. Yang, J. Y. Kim, Y. W. Han, and D. K. Moon, "Facile Strategy for Reducing Cell-to-Module Efficiency Gap in Organic Solar Cells by Controlling the Preaggregation of Photoactive Solutions," *Acs Applied Materials & Interfaces* 17 (2025): 6626.

26. M. Gruber, V. Jovanov, and V. Wagner, "Modeling of Photoactive Area Spreading in Unstructured Photovoltaic Cells," *Solar Energy Materials and Solar Cells* 200 (2019): 110011.

27. E. Jiang, C. Baretzky, D. Müller, O. Fischer, B. Zimmermann, and U. Würfel, "Side Connection for High-Efficiency Organic Photovoltaic Modules for Indoor Applications: Shunt Reduction and Performance Improvement," *Solar Rrl* 8 (2024): 2400303.

28. F. Yang, Y. Huang, Y. Li, and Y. Li, "Large-Area Flexible Organic Solar Cells," *Npj Flexible Electronics* 5 (2021): 30.

29. H. Shekhar, O. Solomeshch, D. Liraz, and N. Tessler, "Low Dark Leakage Current in Organic Planar Heterojunction Photodiodes," *Applied Physics Letters* 111 (2017): 223301.

30. D. R. B. Amorim, D. J. Coutinho, P. B. Miranda, and R. M. Faria, "Analytical Model for Photocurrent in Organic Solar Cells as a Function of the Charge-Transport Figure of Merit including Second-Order Recombination," *Physical Review Applied* 14 (2020): 034046.

31. D. Lübke, P. Hartnagel, M. Hülsbeck, and T. Kirchartz, "Understanding the Thickness and Light-Intensity Dependent Performance of Green-Solvent Processed Organic Solar Cells," *Acs Materials Au* 3 (2023): 215.

32. D. Lee, J. Kim, G. Park, H. W. Bae, M. An, and J. Y. Kim, "Enhanced Operating Temperature Stability of Organic Solar Cells with Metal Oxide Hole Extraction Layer," *Polymers* 12 (2020): 992.

33. F. Jamaatisomarin, R. Chen, S. Hosseini-Zavareh, and S. Lei, "Laser Patterning of Photovoltaic Solar Thin Films: A Review," *Journal of Manufacturing and Materials Processing* 7 (2023): 94.

34. H. Li, S. Liu, X. Wu, et al.,"Advances in the Device Design and Printing Technology for Eco-Friendly Organic Photovoltaics," *Energy & Environmental Science* 16 (2023): 76–88.

35. P. Pou-Álvarez, A. Riveiro, X. R. Nóvoa, et al., "Nanosecond, Picosecond and Femtosecond Laser Surface Treatment of Magnesium Alloy: Role of Pulse Length," *Surface & Coatings Technology* 427 (2021): 127802.

36. S. Rung, J. Barth, and R. Hellmann, "Characterization of Laser Beam Shaping Optics Based on Their Ablation Geometry of Thin Films," *Micromachines* 5 (2014): 943–953.

37. Y. Jin, L. Sun, L. Qin, et al., "Solution-Processed Solar-Charging Power Units Made of Organic Photovoltaic Modules and Asymmetric Super-Capacitors," *Applied Physics Letters* 118 (2021): 203902.

Supporting Information

Additional supporting information can be found online in the Supporting Information Section. **Supporting Fig. S1:** CV curves of (a) PM6 and (b) L8-BO films. (c) UV–Vis normalized absorption spectra and (e) energy levels of PM6 and L8-BO films. **Supporting Fig. S2:** (a) Schematic diagrams of OSC modules fabricated by the hand-made method (left) and laser patterning method (right), indicating the aperture area (red box) and the active area (yellow). (b) Photograph (left) and dimensional drawing (right) of the shadow mask used during J–V measurements. **Supporting Fig. S3:** Effect of Q-pulse width (5 μs vs. 10 μs) and scan speed (300 mm s^{-1} vs. 650 mm s^{-1}) on energy distribution and overlap behavior. **Supporting Fig. S4:** Optical microscopy images of P1 lines fabricated with different Q-pulse widths (8–16 μs). **Supporting Fig. S5:** Optical microscopy images of P1 lines fabricated with different scan speeds (200–900 mm s^{-1}). **Supporting Fig. S6:** Optical analysis for optimizing P2 laser scribing with different Q-pulse widths (16, 16.5, and 17 μs): P1 (13 μs). **Supporting Fig. S7:** Light stability (ISOS-L-1) of o-xylene processed OSC modules comparing hand-made and UV laser-patterned devices. **Supporting Table S1:** Photovoltaic parameters for optimizing OSC cells based on PM6 and L8-BO materials. The process variables include solution concentration (6.5 and 7.0 mg mL^{-1}), spin-coating speed (RPM), and thermal annealing conditions. **Supporting Table S2:** Photovoltaic parameters of OSC modules for optimizing P2 laser scribing

with respect to Q-pulse widths. **Supporting Table S3:** Photovoltaic parameters of OSC modules for optimizing P3 laser scribing with respect to Q-pulse widths. **Supporting Table S4:** Comparison of geometry-dependent photovoltaic parameters between hand-made and UV nanosecond laser-patterned OSC modules. **Supporting Table S5:** Photovoltaic parameters of hand-made and laser-patterned OSC modules under low-intensity light from 3,000 K LED. **Supporting Table S6:** Series resistance (R_S) and shunt resistance (Rsh) of the hand-made and UV nanosecond laser-patterned OSC modules measured under different illumination intensities from 1 sun to 200 lux. **Supporting Table S7:** Photovoltaic performance parameters of PM6:L8-BO OSC modules fabricated by hand-made and UV nanosecond laser patterning methods using o-xylene. **Supporting Table S8:** Summary of reported OSC and PSC modules with aperture/active area, laser details, sub-cell number, dead zone, GFF, and PCE.